



# 1           **Unravelling Landslide Failure Mechanisms with Seismic Signal**

## 2                           **Analysis for Enhanced Pre-Survey Understanding**

3   Jui-Ming Chang<sup>1,2</sup>, Che-Ming Yang<sup>3\*</sup>, Wei-An Chao<sup>1,2</sup>, Chin-Shang Ku<sup>4</sup>, Ming-Wan Huang<sup>3,5</sup>, Tung-  
4   Chou Hsieh<sup>2</sup>, Chi-Yao Hung<sup>6</sup>

5  
6   <sup>1</sup>Department of Civil Engineering, National Yang Ming Chiao Tung University, Hsinchu 30010, Taiwan

7   <sup>2</sup>Disaster Prevention and Water Environment Research Center, National Yang Ming Chiao Tung  
8   University, Hsinchu 30010, Taiwan

9   <sup>3</sup>Department of Civil and Disaster Prevention Engineering, National United University, Miaoli 36063,  
10   Taiwan

11   <sup>4</sup>Institute of Earth Sciences, Academia Sinica, Taipei 11529, Taiwan

12   <sup>5</sup>He Yu Engineering Consultants Co. Ltd., Taichung 40642, Taiwan

13   <sup>6</sup>Department of Soil and Water Conservation, National Chung Hsing University, Taichung 40227, Taiwan

14   *Correspondence to:* Che-Ming Yang ([stanleyyangcm@nuu.edu.tw](mailto:stanleyyangcm@nuu.edu.tw))

15



## 16 **Abstract**

17 Seismic signals, with their remote and continuous monitoring advantages, have been instrumental in  
18 unveiling various landslide characteristics and have been widely applied in the past decades. However, a  
19 few studies have extended these results to provide geologists with pre-survey information, thus enhancing  
20 the understanding of the landslide process. In this research, we utilize the deep-seated Cilan Landslide  
21 (CL) as a case study and employ a series of seismic analyses, including spectrogram analysis, single force  
22 inversion, and geohazard location. These techniques enable us to determine the physical processes, sliding  
23 direction, mass amount estimation, and location of the deep-seated landslide. Through efficient discrete  
24 Fourier transform for spectrograms, we identified three distinct events, with the first being the most  
25 substantial. Further analysis of spectrograms using a semi-log frequency axis generated by discrete  
26 Stockwell transform revealed that Event 1 consisted of four sliding failures occurring within thirty  
27 seconds with decreasing sliding mass. Subsequent Events 2 and 3 were minor toppling and rockfalls,  
28 respectively. Geohazard location further constrained the source location, indicating that Events 1 and 2  
29 likely originated from the same slope. Subsequently, the sliding direction retrieved from single force  
30 inversion and volume estimation was determined to be  $153.67^\circ$  and  $557,118 \text{ m}^3$ , respectively, for the CL.  
31 Geological survey data with drone analysis corroborated the above seismological findings, with the  
32 sliding direction and source volume estimated to be around  $148^\circ$  and  $664,926 \text{ m}^3$ , respectively, closely  
33 aligning with the seismic results. Furthermore, the detailed dynamic process observed in the spectrogram  
34 of Event 1 suggested a possible failure mechanism of CL involving advancing, retrogressing, enlarging,  
35 or widening. Combining the above mechanism with geomorphological features identified during field  
36 surveys, such as the imbrication-like feature in the deposits and the gravitational slope deformation, with  
37 event video, infers the failure mechanism of retrogression of the Event 1 after shear-off from the toe.  
38 Then, the widening activity was caused by the failure process for subsequent events, as Events 2 and 3.  
39 This case study underscores the significance of remote and adjacent seismic stations in offering  
40 seismological-based landslide characteristics and a time vision of the physical processes of landslides,  
41 thereby assisting geologists in landslide observation and deciphering landslide evolution.

42 **Keywords:** Cilan Landslide, Spectrograms, Discrete Stockwell Transform, Landslide Failure Mechanism



## 43 **1 Introduction**

44 In recent decades, seismology has expanded in scope to include mass movements on the Earth's  
45 surface since the first observation of landslide signals during volcanic eruptions (Kanamori and Given,  
46 1982). After that, the application of associated analyses from seismology, particularly in landslide  
47 research has gradually increased (Brodsky et al., 2003; Vilajosana et al., 2008; Feng, 2011; Allstadt et al.,  
48 2013; Hibert et al., 2014; Dietze et al., 2017).

49 Different seismic signal frequencies play distinct roles in landslide characterization. Low-  
50 frequency seismic signals, typically below 0.1 Hz, have been employed to approximate the source location,  
51 estimate the sliding direction, and reconstruct its trajectory (Yamada et al., 2013; Hibert et al., 2015; Chao  
52 et al., 2018). These signals are generated by ground rebound from slope failure, which were detected in  
53 the cases of massive landslides with areas greater than 10,000 m<sup>2</sup> or volumes exceeding 100,000 m<sup>3</sup> (Kuo  
54 et al., 2018). Moreover, low-frequency signals have unique characteristics that can be used as  
55 distinguishing features. The signal source is assumed to be a point source that undergoes loading and  
56 unloading processes. By comparing synthetic and observed waveforms from a single force mechanism  
57 using a grid search and by adapting data from seismic stations, the approximate source location and  
58 inverted force direction of a landslide can be determined (Chao et al., 2017). The magnitude of the  
59 inverted force is related to the landslide scale (Ekström and Stark, 2013; Chao et al., 2016). However,  
60 because of the longer wavelengths associated with low-frequency signals, the accuracy of the source  
61 constraints is reduced compared to higher-frequency signals.

62 High-frequency seismic signals (>1Hz) have different functions in landslide research. They are,  
63 for example, used to recognize the details of the source mechanism (Provost et al., 2018; Weng et al.,  
64 2022) and the constraints of the source location (Chen et al., 2013; Walsh et al., 2017; Yang et al., 2022).  
65 Seismic time-frequency spectrograms have been identified as the source type. Compared with the right  
66 triangle spectrogram feature associated with the onset of the P-wave of earthquakes, landslides typically  
67 exhibit a cigar-shaped feature with a linear (Suriñach et al., 2005; Moretti et al., 2012) or semi-log  
68 (Dammeier et al., 2011) frequency axis resulting from the Fourier transform. More recently, other  
69 spectrogram features, such as V-shaped, column-shaped, and pulse-like features corresponding to the



70 failure mechanisms of sliding, toppling, and rockfall, respectively (Chang et al., 2021) have been observed  
71 in spectrograms generated by the Stockwell transform with a semi-log plot. However, the advantages and  
72 disadvantages of these two linear and semi-log label transforms have not been thoroughly addressed.  
73 Through spectrogram recognition, the duration of the physical processes of a landslide can be determined.

74 There are three methods used for the source location: (1) time difference (Chen et al., 2013; Fuchs  
75 et al., 2018; Manconi and Mondini, 2022), (2) amplitude decay (Aki and Ferrazzini, 2000; Walter et al.,  
76 2017), and (3) the azimuth of polarization analysis (Guinau et al., 2019). The time-difference method  
77 calculates the time difference between pairs of stations using a velocity model to constrain possible source  
78 locations. The accuracy of location determination depends upon the station coverage of the source area  
79 (Chang et al., 2023). The amplitude source location method considers the decay of the seismic amplitude  
80 with distance. However, the results can be influenced by the distribution of the source-station distances,  
81 which often leads to the source location being biased toward the station with the highest amplitude caused  
82 by site effect (Chang et al., 2023). Although the first and second methods are commonly used in landslide  
83 research, the azimuth of polarization analysis has rarely been discussed in landslide source analysis.  
84 Guinau et al. (2019) adapted the polarization to retrieve the source azimuth and locate the rockfall by  
85 recognizing P- and S-waves through particle motion.

86 Investigations into low- and high-frequency seismic signals provide invaluable perspectives on  
87 landslides. However, few studies have sorted out the information as preliminary knowledge to geologists,  
88 especially for the continuous time vision of the failure process. Historically, geologists relied solely on  
89 field and drone surveys conducted before and after landslide events to depict landslide failure mechanisms,  
90 thereby lacking associated information on temporal evolution to link different phases of landslide activity.  
91 Geologists need to speculate on the connection of landslide activity to the geological model. However,  
92 seismological-based information complements this approach by providing temporal context. Therefore,  
93 this study integrates seismic results with landslide investigation (field and drone surveys) to illustrate  
94 constructing a landslide evolution model.

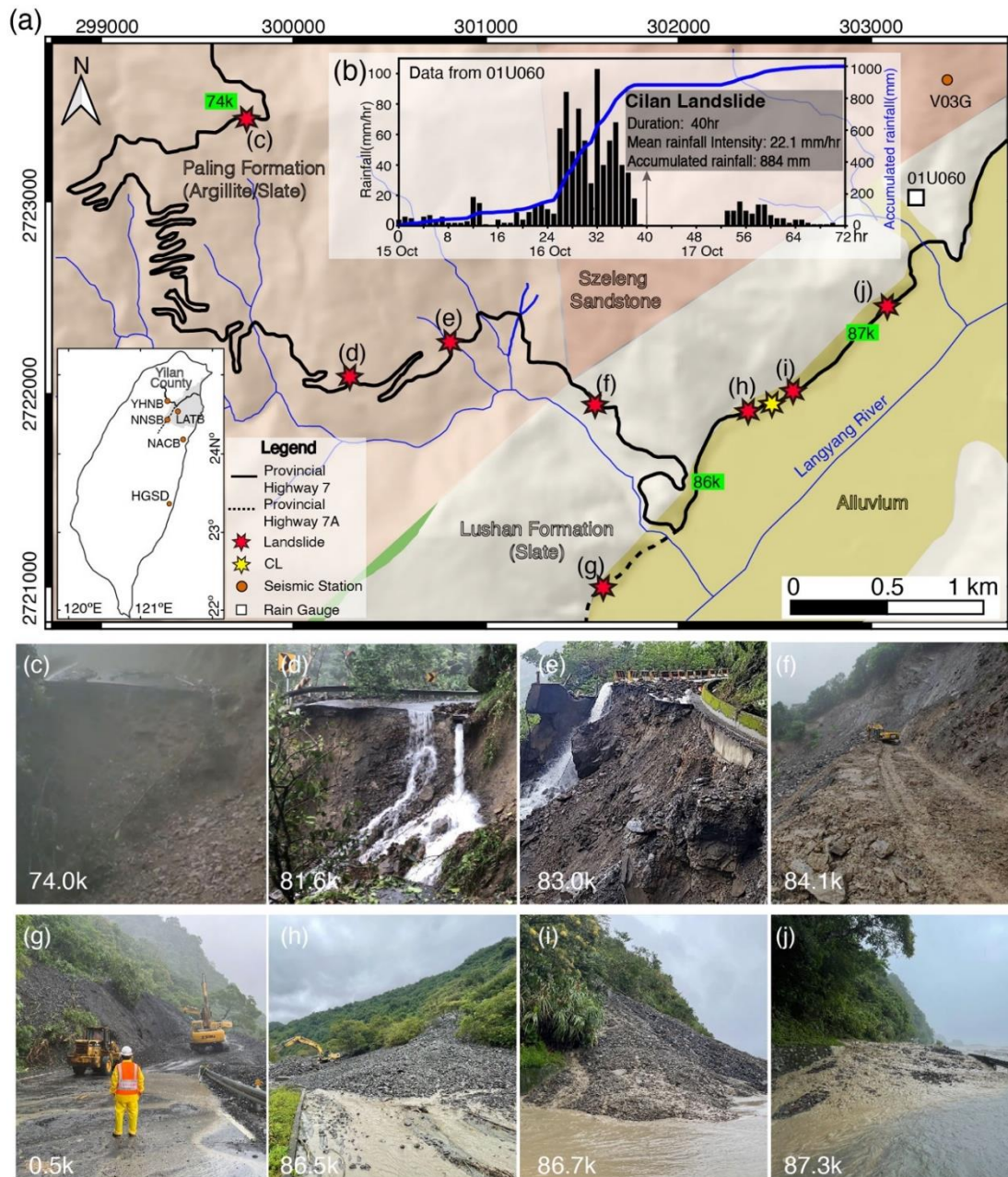
95



## 96 **2 Background information**

### 97 **2.1 Landslides During Typhoon Nesat**

98           Torrential rainfall resulting from the interaction between Typhoon Nesat and the winter monsoon  
99 lashed Yilan County in northeast Taiwan from 15 October to 17 October 2022 (Fig. 1a; the time in this  
100 research all shows in local time UTC+8). The accumulated precipitation reached 1,000 mm in three days,  
101 with a peak rainfall intensity of 103 mm hr<sup>-1</sup>. (Fig. 1b). This accumulation exceeded the landslide  
102 threshold of 550 mm, as documented by the Agency of Rural Development and Soil and Water  
103 Conservation (<https://246.ardswc.gov.tw/>; last accessed on 4 April 2024). Consequently, many rainfall-  
104 induced landslides occurred, destroying sections of two vital provincial highways: No. 7 (Northern Cross-  
105 Island Highway) and No. 7A (Fig. 1a). The Directorate General of Highways, Taiwan, reported nine  
106 sections damaged by landslides (Figs. 1c-1j; Table S1). Among these, three roadbed washouts  
107 characterized by argillite/slate were observed in the Paling Formation (Figs. 1c-1e), whereas a landslide  
108 composed of slate covered a road section in the Lushan Formation (Fig. 1f). Additionally, four debris  
109 flow events occurred near the boundary between the Lushan Formation and the alluvium (Figs. 1g-1j).  
110 As of 22 October 2022, these events left 302 people stranded, resulting in one missing person. In addition  
111 to these nine events, a deep-seated landslide, known as the Cilan landslide (CL), occurred in the Lushan  
112 Formation. Initially, an individual captured a part of the CL process on video, revealing two distinct stages  
113 of material sliding (Fig. S1). According to the video footage, the initial landslide was formed by exposure  
114 to the bare earth. The video captured the subsequent failures. The first body in the footage slid between  
115 0-20 seconds, and the following failure occurred at the 20-second mark in the video recording. Then, the  
116 Directorate General of Highways in Taiwan identified the precise location of the landslide (Fig. S2 and  
117 yellow star in Fig. 1a) and provided an approximate occurrence time of 4:00 PM on 16 October 2022.



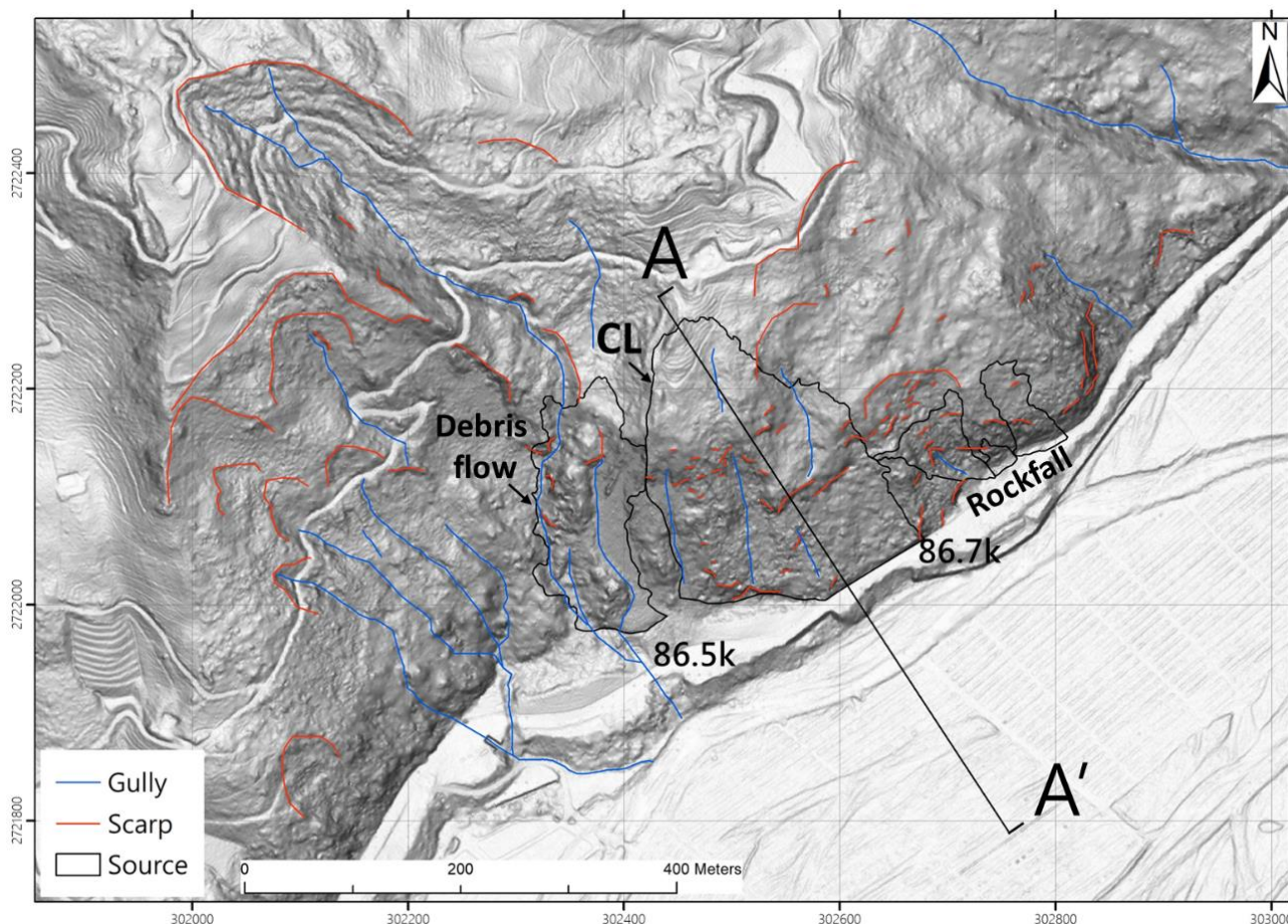
118

119 Figure 1 (a) Regional geologic map of roadside landslides, seismic station, and rain gauge (Fei and Chen,  
120 2013). The grey-shaded area in the map of Taiwan (lower left) represents Yilan County. (b) Rainfall data  
121 of rain gauge 01U060 during the typhoon. The rain episode started on 15 October 2022 at 00:00 AM  
122 (Local time UTC+8). (c)-(j) In situ photos for landslides. All photos are open data from the Directorate  
123 General of Highways, Taiwan (Table S1). The k in the map/photos indicates the milestone (in kilometers)  
124



## 125 2.2 Topographic Feature Near the CL

126 According to 1-m high-resolution LiDAR-derived slope inclination map (Fig. 2), several  
127 prominent features were evident near the CL. On the west side of the CL, a concave slope displayed  
128 distinct scarps and gullies. These features strongly indicated that the concave slope was subject to erosion.  
129 Conversely, the eastern roadside slopes of the CL revealed a contrasting topography characterized by  
130 numerous scarplets with several gullies and convex slopes, all prone to rockfalls. Within this context,  
131 slopes at the 86.5 km and 86.7 km milestones along Provincial Highway No. 7 experienced a debris flow  
132 on the gentler portions (Fig. 1h) and talus deposits on the steeper sections (Fig. 1i).

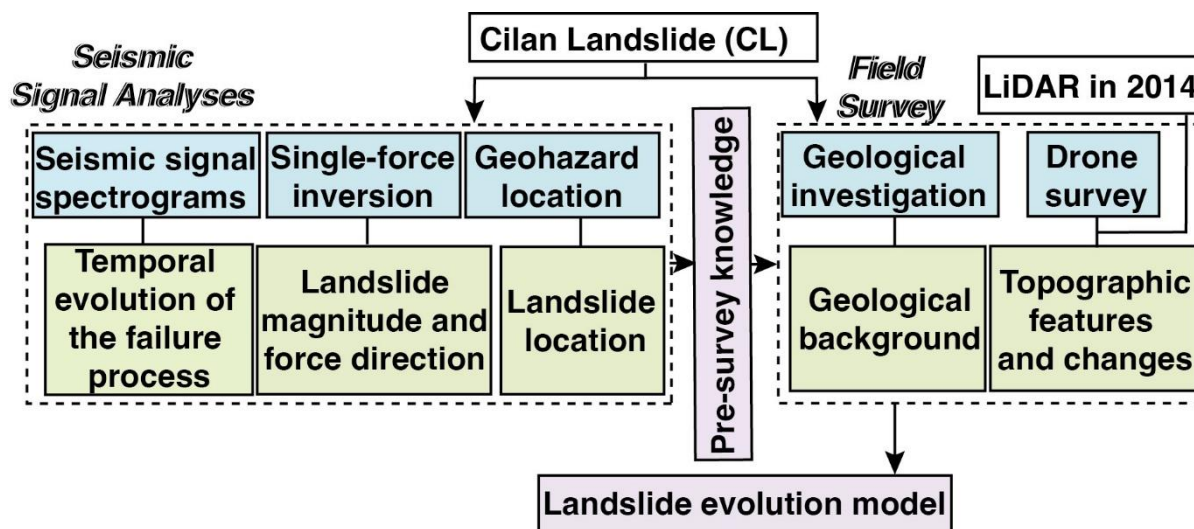


133 Figure 2 Topographic feature interpretation with 1 m high-resolution LiDAR slope map in 2014 before  
134 the CL. The AA' is for the topographic profile in Fig. 7b. The black line polygons indicate the  
135 source boundary of slope failures.  
136



137 **3. Methods**

138 The study aims to leverage seismic analysis as preliminary knowledge to aid in illustrating the  
 139 landslide evolution model of the CL. To achieve this, we conducted a series of seismic signal analyses,  
 140 including seismic signal spectrograms, single force inversion (SF), and geohazard location (GeoLoc).  
 141 These analyses provide insights into the temporal evolution of the failure process, landslide magnitude,  
 142 inverted force direction, and landslide location constraints. Geologists use these results to gain a basic  
 143 understanding of the CL prior to conducting a field survey. The field survey consists of two parts:  
 144 geological investigation and drone survey. The former provides geological background information,  
 145 while the latter joining LiDAR in 2014 captures topographic features and changes post-CL. The combined  
 146 results from the seismic signal analyses and field surveys support the development of the most plausible  
 147 landslide evolution model. The flowchart is depicted in Fig. 3.



148 Figure 3 Flowchart of this study. The blue, green, and purple backgrounds are relevant to the methodology,  
 149 results, and discussion.

151





### 152 3.1 Seismic signal spectrograms

153 The study investigated time-frequency spectrograms based on the power spectral density (PSD)  
154 of the discrete Fourier transform (DFT), as well as the power spectrum (PS) of the discrete Stockwell  
155 transform (DST). The DST of Eq. (1) was derived from Eq. (2), while  $f$ ,  $\tau$ ,  $t$ , and  $\alpha$  were derived from Eqs.  
156 (3)-(7).

$$157 \text{ DST: } s[p\Delta t, \frac{l}{N\Delta t}] = \sum_{m=1}^{N-1} H[\frac{l+m}{N\Delta t}] e^{-2\pi^2 \frac{m^2}{l^2}} e^{2\pi i \frac{mp}{N}} \quad (1)$$

$$158 \text{ DFT: } H[\frac{l}{N\Delta t}] = \frac{1}{N} \sum_{k=0}^{N-1} h[k\Delta t] e^{-2\pi i \frac{lk}{N}} \quad (2)$$

$$159 f = \frac{l}{N\Delta t}, \quad l = 0, 1, 2 \dots N - 1 \quad (3)$$

$$160 \tau = p\Delta t, \quad p = 0, 1, 2 \dots N - 1 \quad (4)$$

$$161 \alpha = \frac{m}{N\Delta t}, \quad m = 0, 1, 2 \dots N - 1 \quad (5)$$

$$162 t = k\Delta t, \quad k = 0, 1, 2 \dots N - 1 \quad (6)$$

$$163 PS = s[p\Delta t, \frac{l}{N\Delta t}]^2 \quad (7)$$

164 where  $\Delta t$  is the time sample interval,  $\tau$  denotes the time of spectral localization,  $N$  is the total number of  
165 data points,  $\alpha$ , and  $f$  control the discrete frequency point, and  $h[t]$  is the discrete-time series seismic data.

166 In the context of landslides, the predominant frequencies of ground vibrations typically range from  
167 1 Hz to 10 Hz (Chang et al., 2021). To represent the power distribution within this range precisely, we  
168 configured the DFT analysis to have time and frequency resolutions of 1.28 seconds and 0.39 Hz,  
169 respectively. This configuration effectively captured the pertinent frequency information while retaining  
170 an acceptable time resolution. Also, a cumulative PSD plot was obtained by summing the PSD values at  
171 discrete time intervals. Alternately, applying DST instead of DFT allows for either enhanced frequency  
172 resolution for the lower frequencies through broader time windows or improved time resolution for the  
173 higher frequencies through narrower windows. In this study, we opted for a time window of 0.05 seconds  
174 and a frequency resolution of 0.30 Hz in the DST analysis. These parameters provided superior frequency  
175 and time resolutions, enabling the capture of intricate spectrogram details.



176 The scale of the frequency axis on the spectrograms profoundly influences recognition and  
177 interpretation within the target frequency range of 1 Hz to 10 Hz. Therefore, we incorporated linear and  
178 logarithmic frequency axes into the spectrograms. By judiciously selecting window lengths, time and  
179 frequency resolutions, and frequency axes, we facilitated effective visualization and analysis of the power  
180 distribution in seismic signals, particularly within the frequency range pertinent to landslide occurrences.

### 181 **3.2 Single-force inversion (SF)**

182 Single-force inversion (SF) is a technique used in the near-real-time landquake monitoring system  
183 (NRLAMS) (Chao et al., 2017) to extract the possible force direction and magnitude of a landslide. Before  
184 conducting the SF analysis, we performed several preprocessing steps on the seismic signals. First, we  
185 applied a bandpass filter between 0.02 Hz and 0.05 Hz to isolate the frequency range for large-scale  
186 landslides (volume  $> 10^5 \text{ m}^3$  or area  $> 10^4 \text{ m}^2$ , as defined by Chen, 2015). This frequency range is  
187 associated with landslide-related signals in Taiwan (Chao et al., 2017). In addition, we transformed the  
188 original horizontal components of the seismic data into radial and tangential components. Different  
189 weightings in the SF correspond to the signal-to-noise ratio (SNR) (Table S2), the ratio between the  
190 absolute peak amplitude and the average absolute amplitude from the entire signal trace.

191 Subsequently, the SF analysis simulated synthetic waveforms assuming a source depth of 1 km,  
192 and Green's functions were calculated based on the surface wave velocity model proposed by Shin and  
193 Chen (1998). Different synthetic waveforms were generated using different settings of force direction,  
194 magnitudes, and dips. These waveforms were compared with the observed signals regarding fitness values,  
195 the sum of the maximum normalized cross-correlation coefficient, and variance reduction. The highest  
196 fitness values corresponding to the inverted force parameters were determined. Furthermore, a parameter  
197 of inverted force magnitude (unit: Newton) of SF could be used to estimate the landslide mass through  
198 the empirical formula, mass (kg) =  $0.405 \times$  force magnitude (Chao et al., 2016). Assuming a rock density  
199 of approximately  $2,600 \text{ kg m}^{-3}$ , the estimated landslide mass could be roughly converted to landslide  
200 volume. The seismic data for the SF analysis were obtained from a broadband array in Taiwan for seismic  
201 networks (Kao et al., 1998). A more detailed methodology associated with the parameter setting and  
202 procedure is provided by Chao et al. (2017).



### 203 **3.3 Geohazard location**

204 The geohazard location (GeoLoc) method, as outlined by Chang et al. (2021), synergizes the cross-  
205 correlation (CC) method (Chen et al., 2013) with the amplitude source location (ASL) method (Aki and  
206 Ferrazzin, 2000) to pinpoint potential landslide locations using seismic signals in the frequency range of  
207 over 1 Hz. This approach initially filtered the seismic data between 1 Hz and 3 Hz. Subsequently, the  
208 SNR was calculated as a ratio between the short-term average ( $\pm 5$  s from the maximum envelope  
209 amplitude) and the long-term average of a 180-second target trace. A threshold of SNR larger than 1.7  
210 was applied to select the available waveforms for further analysis. The selected frequency range and SNR  
211 threshold were empirically established based on extensive-scale landslides in Taiwan (Chen et al., 2013).

212 The CC method calculates the maximum cross-correlation coefficient between each station pair  
213 to extract the travel time difference. This difference was then used with a three-dimensional velocity  
214 model (Wu et al., 2007) and grid search to define the misfit function. Simultaneously, the ASL method  
215 gauges its misfit function by optimizing the fit of the amplitude decay curve. By individually sorting the  
216 misfit functions across all search grids, both methodologies yielded reliable source locations for landslides.  
217 The potential source locations were identified when the grids had relative fitness values greater than 0.95  
218 Chang et al. (2023). The detailed algorithm of GeoLoc can be found in Chang et al. (2021).

219 Seismic data for GeoLoc analysis were collected from various sources (Table S3), including  
220 temporary stations maintained by the Comprehensive Landquake Monitoring Lab (CoLLab), National  
221 Yang Ming Chiao Tung University, a broadband array in Taiwan for seismology, and the Central Weather  
222 Administration, Taiwan.

### 223 **3.4 Field survey**

224 The field survey encompassed two integral components: drone survey and geological  
225 investigation. For the drone survey, we conducted a series of vertical and inclined aerial photos along the  
226 CL using the DJI Phantom 4. These photos were input for the photogrammetry software Pix4D, which  
227 generated a digital surface model (DSM). Through the DSM, the geomorphological features after the CL  
228 could be depicted. Additionally, by combining the LiDAR data from 2014 with DSM, we could observe



229 the differences in topography before and after the CL event. On the other hand, the geological  
230 investigation focused on road inspection and outcrop observation before and after the CL, respectively.  
231 The road inspection documented the status of slope protection, particularly regarding crack geometry.  
232 The outcrop observation recorded the strike and dip for cleavage, joints, and bedding near the CL.

## 233 **4. Result**

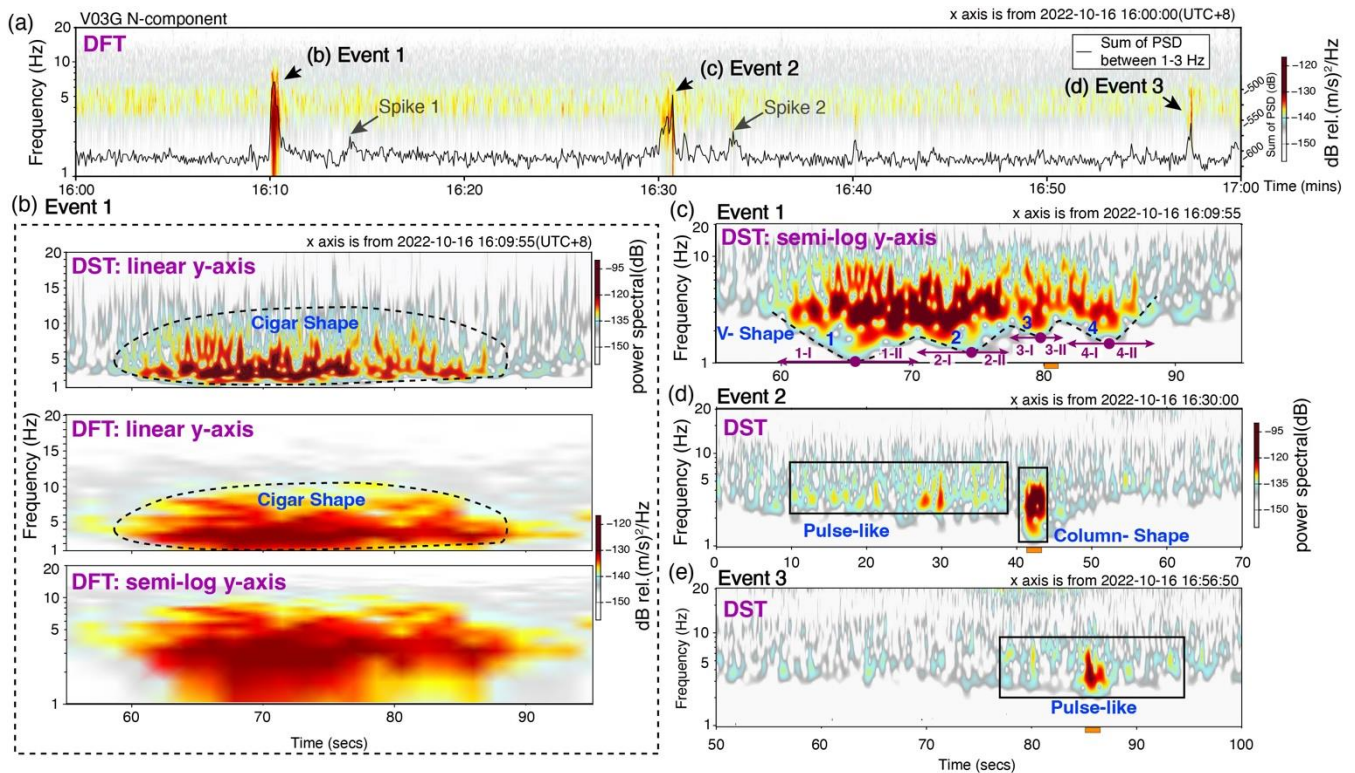
### 234 **4.1 Seismic spectrograms for the CL**

235 According to the one-hour spectrogram generated through DFT analysis of V03G (Fig. 4a), the  
236 resulting spectrograms revealed three distinct high-power onsets potentially corresponding to different  
237 landslide events. The first event, labeled Event 1, occurred from 16:10:00 to 16:10:30. The cigar-shaped  
238 features of the spectrograms indicated a landslide process when the spectrograms were analyzed using a  
239 linear frequency axis (Fig. 4b). However, when the DST was modified to a semi-log graph, the lower  
240 bounds of the high PSD displayed V-shaped spectrogram features (Fig. 4c). Such V-shaped patterns were  
241 not discernible in the spectrograms obtained using the DFT because of the inherent limitations imposed  
242 by the frequency and time resolution (Fig. 4b). The V-shape is associated with sliding behavior (Chang  
243 et al., 2021), which involves phases of acceleration and deceleration of the landslide materials separated  
244 by the lowest point of the V-shape. In Event 1, the four V-shaped events were interconnected, and their  
245 lowest points (depicted as purple dots in Fig. 4c) gradually shifted to higher frequencies, indicating a  
246 reduction in the sliding material volume. As a result, the most significant event was the initial sliding of  
247 massive mass, which also generated signals within the frequency range of 0.02 Hz to 0.05 Hz, detectable  
248 by the SF method (See following subsection). With smaller volumes involved in the subsequent sliding  
249 events, the corresponding signals in the low-frequency range could not be generated.

250 Approximately 20 min after Event 1, Event 2 occurred, and the spectrogram revealed a sequence  
251 of continuous pulse-like features (black rectangle in Fig. 4d). However, the frequency bands associated  
252 with these pulse-like features overlapped with ambient noise. Certain pulse-like features could be  
253 discerned, indicating continuous rock-ground impacts in the form of rockfalls. Subsequently, a column-  
254 like shape emerged in the spectrogram, an interaction between the substantial mass and the slope or  
255 ground (dashed black rectangle in Fig. 4d). This phenomenon referred to processes such as toppling or



256 rockfalls on overhanging slopes or similar mechanisms. Approximately 26 min later, Event 3 emerged,  
 257 presenting spectrogram features analogous to the continuous rock-ground impacts observed in Event 2  
 258 (black rectangle in Fig. 4e). In particular, a gradual decrease in the PSD and PS values and signal durations  
 259 was evident from Events 1 to 3, presenting a reduction in the scale of the landslide.



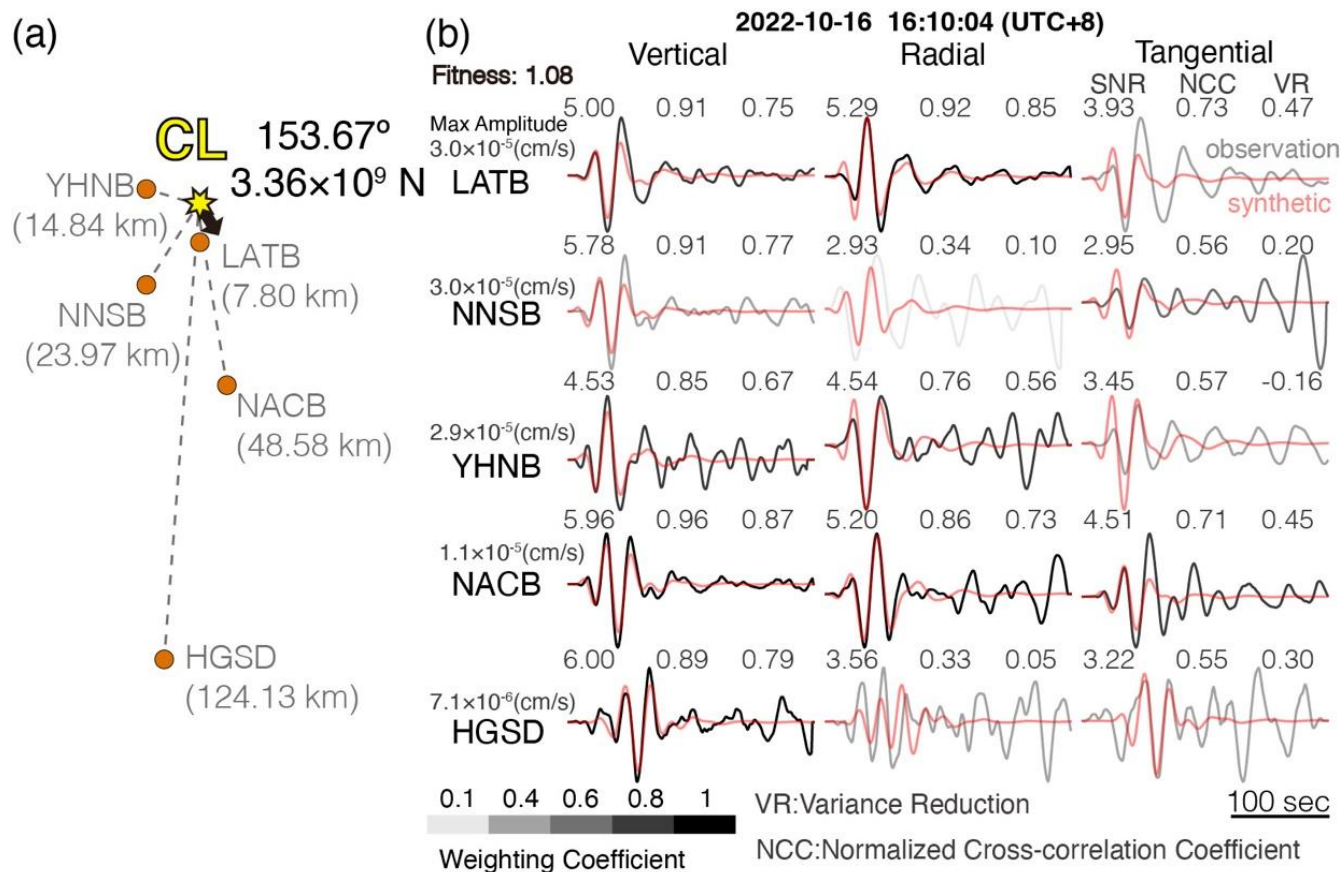
260  
 261 Figure 4 Spectrograms of the seismic signal from V03G with the North component. (a) DFT spectrogram  
 262 and PSD sum between 16:00-17:00 on 16 October 2022 (UTC+8). (b) Event 1 of DST with linear  
 263 frequency axis and DFT with linear frequency and semi-log frequency axes. (c) DST spectrogram with  
 264 semi-log frequency axes for Event 1. The black dashed line is the lower boundary of the high PS values,  
 265 showing the V-shaped spectrogram feature. The purple points are the lowest points of the four V-shapes  
 266 that separate the first half (I), the acceleration phase, from the second half (II), the deceleration phase.  
 267 The blue numbers indicate a sequence of the V-shapes. (d) Spectrogram of DST for Event 2. The black  
 268 rectangles mark the spectrogram feature. (e) DST spectrogram for Event 3. The horizontal orange bars  
 269 below the x-axis in (c)(d)(e) are the signal windows for particle motion analysis in Fig. 10.



270           Except for Events 1 to 3, Fig. 4a exhibited two spikes. We examined the corresponding  
271 spectrograms and found that the signals were faint and heavily obscured by ambient noise (Fig. S3).  
272 Consequently, the evidence derived from these indirect observations does not substantiate their origin  
273 from landslide activity.

#### 274 **4.2 Single-force inversion for the CL**

275           We employed an SF approach for Event 1 of the CL, utilizing a network of five seismic stations  
276 (Fig. 5a). Source-station distances spanned from 7.80 km to 124.13 km, and back azimuths ranged from  
277 170° to 296°. After testing several starting times of the seismic signals for the SF, we found that signals  
278 starting at 16:10:04 yielded the best results. The normalized cross-correlation coefficient and the variance  
279 reduction of these signals averaged 0.72 and 0.74, respectively (Fig. 5b). The overall performance  
280 exhibited a fitness value 1.08. Subsequently, the SNR values ranged from 2.93 to 6.00, and the NACB  
281 consistently exhibited a relatively high SNR across the three components. The inversion process yielded  
282 a force direction of 153.67° and a force magnitude of  $3.36 \times 10^9$  (Newton). The magnitude of the force was  
283 converted into landslide mass using an empirical formula, and the landslide volume was estimated to be  
284 approximately 523,540 m<sup>3</sup>.



285

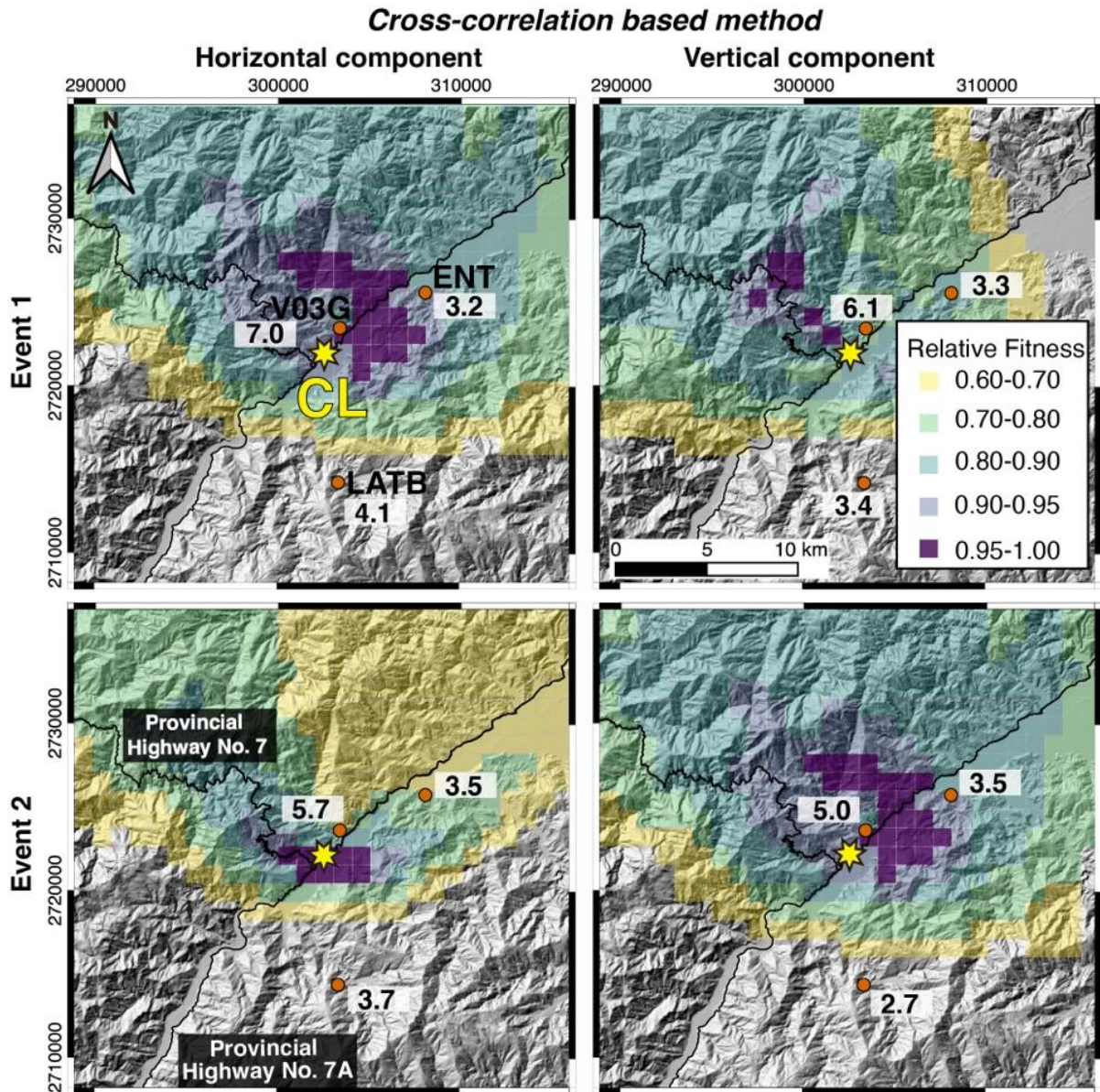
286 Figure 5 (a) Position of seismic stations relative to the CL. The black arrow indicates the inverted force  
 287 direction of 153.67° with a force magnitude of  $3.36 \times 10^9$  (Newton). (b) Synthetic and observation  
 288 waveforms of the CL with SNR, normalized cross-correlation coefficient, and variance reduction. The  
 289 grey gradient presents the different weightings to retrieve the fitness corresponding to the SNR of the  
 290 signals (Table S2).

### 291 4.3 Source location

292 The V03G station recorded Events 1 to 3. When these signals originated from the same slope of  
 293 landslides, the characteristics of the spectrogram could provide valuable insights into the short-term  
 294 behavior of the CL. Therefore, to determine the locations of Events 1 to 3, we utilized the GeoLoc method.  
 295 The results of Events 1 and 2 of the CC, considering both the horizontal and vertical components,  
 296 indicated that the grids with high fitness values ( $> 0.95$ ) were close to the V03G station (Purple grid cells  
 297 in Fig. 6). In addition, the ASL tended to be near the station with the highest amplitude (Fig. S4).



298 Therefore, Events 1 and 2 probably originated from the same landslide location. For Event 3, the signals  
299 were too weak to be detected by the ENT and LATB stations. Only V03G recorded its signals, which  
300 supports the location of Event 3 near the V03G station.



301

302 Figure 6 Location determination by cross-correlation-based method of horizontal and vertical component  
303 data for Event 1 and Event 2. The values following the stations with transparent white backgrounds are  
304 SNR.



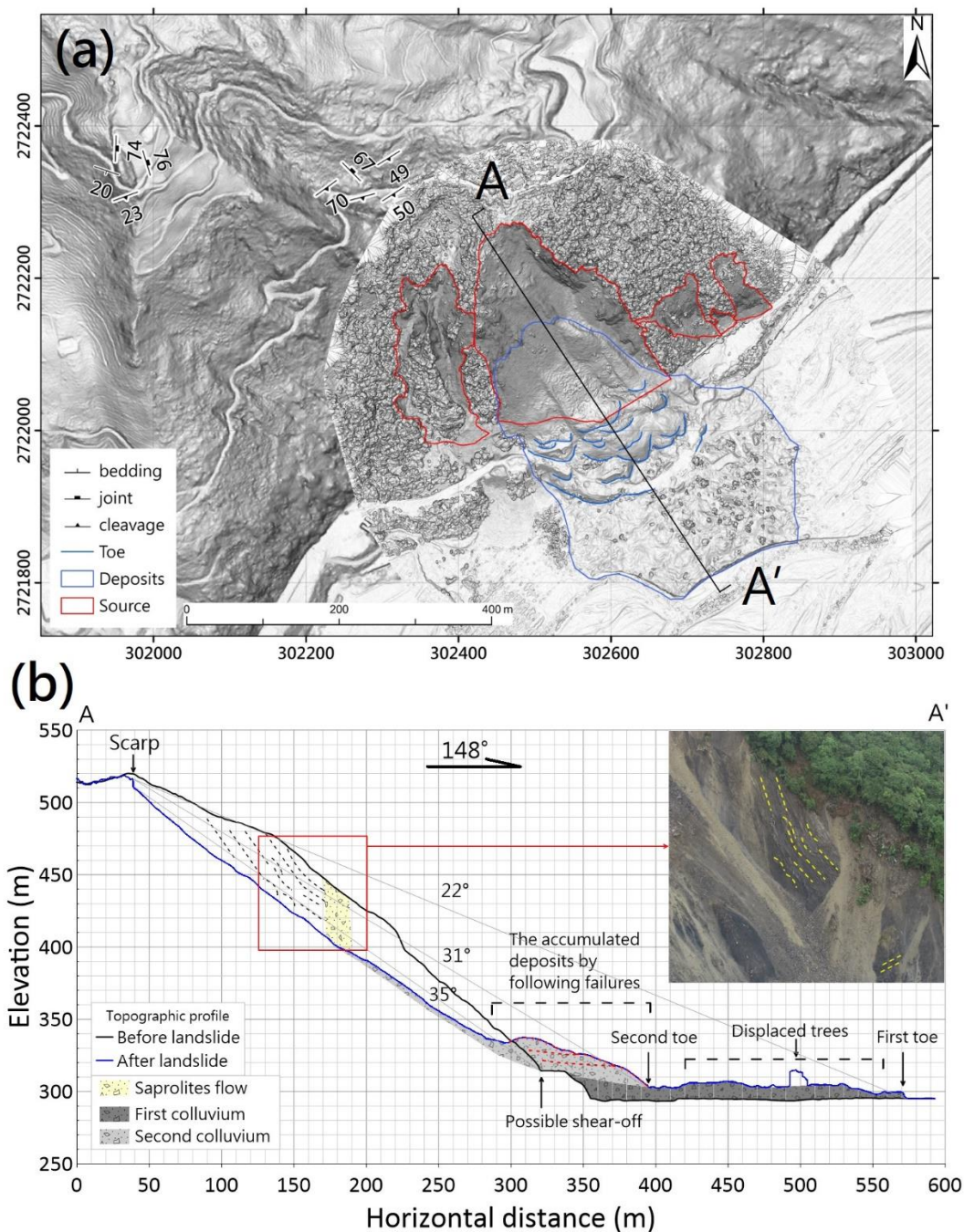


#### 305 **4.4 Landslide survey**

306 According to the topographic profile (A-A' in Fig. 7a), the sliding direction was approximately  
307 148°, similar to the result obtained from the SF (153.67°). The observed elevation difference and travel  
308 distance of the CL were 220 m and 530 m, respectively. The apparent friction angle ranged from 22° to  
309 31°, transitioning from the main scarp to the first significant and subsequent failures (Fig. 7b). This  
310 variation could be attributed to the depositional environments and landslide volumes.

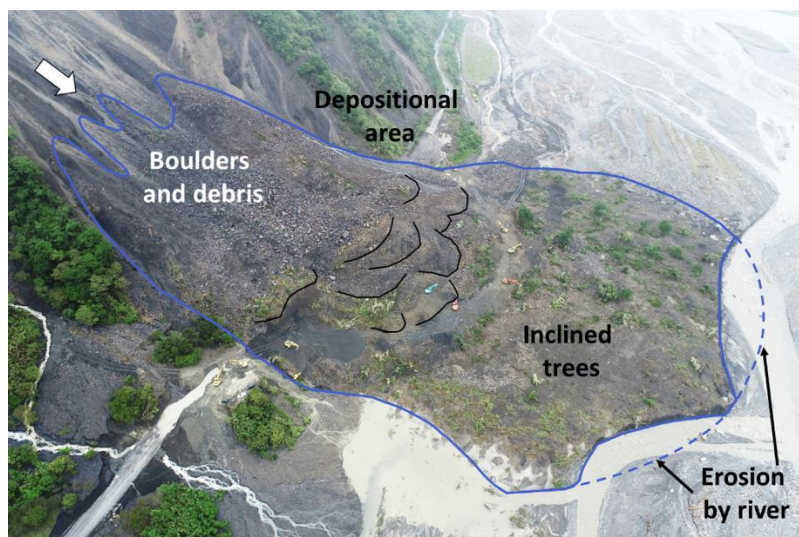
311 Furthermore, we compared the topographical profiles before (1m high-resolution LiDAR data in  
312 2014) and after (DSM by drone) the CL. The data revealed that the maximum erosion depth approached  
313 approximately 45 m near the left flank of the CL, where the bedrock was exposed. For the location,  
314 photographic evidence shows that the dips of slate cleavage exhibited a gradual transition from steep (at  
315 the top) to gentle (at the bottom) (Fig. 7b). This characteristic indicated gravitational slope deformation  
316 (Chigira, 1992; Agliardi et al., 2001), suggesting a weakening of the structural integrity and strength of  
317 the rock mass constituting the slope. The CL originated from a source area measuring 44,562 m<sup>2</sup> and was  
318 deposited over an area of 94,396 m<sup>2</sup>, resulting in a maximum colluvium thickness of 30 m (Fig. 7b). The  
319 calculated source volume by difference of elevation was approximately 664,926 m<sup>3</sup>. Consequently, the  
320 landslide mass was converted into a deposited volume of 690,445 m<sup>3</sup>.

321 The slope map of DSM exhibited deposits with imbrication-like features at the landslide toe,  
322 which was covered on the wider and flatter colluvium with the first toe. This pattern was contributed to  
323 by the widespread colluvium area where numerous trees rest on the colluvium, composed of slate boulders,  
324 debris, saprolites, and soils (Figs. 7b and 8). The inclined trees on the colluvium imply the colluvium is  
325 displaced with slight disturbance due to the low-friction basal detachment. The imbricated deposits near  
326 the original roadside slope represented a depositional sequence resulting from later failures. The result of  
327 the geological investigation shows that the dip direction of the slate cleavage corresponded to the slope  
328 aspect and sliding direction, with a high dip angle influencing CL failure (Fig. 7b). Additionally, before  
329 the occurrence of the CL, an inspection conducted in May 2022 revealed slight damage and displacement  
330 of the downslope concrete wall near the slope (Figs. 9a-9e). These damage signs served as early indicators  
331 of creeping slope.



332

333 Figure 7 (a) Topographic feature interpretation on drone-based slope map after landslide (19 October  
334 2022). (b) Topographic profile of AA'. The embedded drone photos show the slate outcrop on the left  
335 flank of the landslide. The dashed curves indicate that the dip angle and traces of cleavages changed and  
336 deformed.



337

338 Figure 8 The closed aerial photo of CL deposits. The imbrication-like features are linedated by black lines.  
339 The first toe was eroded by river.



340

341 Figure 9 (a) © Google Earth image before the CL. (b)-(e) Photos from inspection on 27 May 2022. (f) Drone-  
342 based 3-dimensional model after the CL. (g)-(j) Photos of crown cracks of the CL.

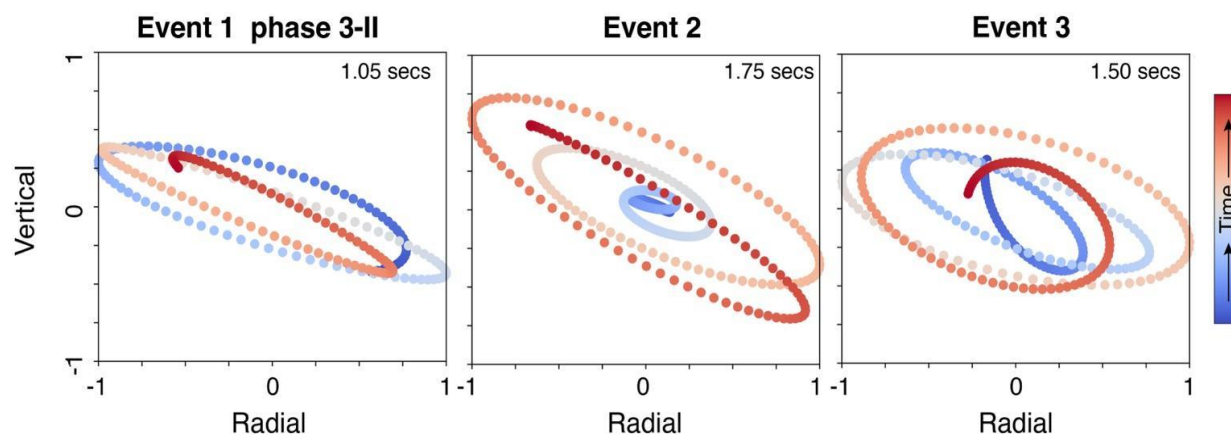


## 343 **5. Discussion**

### 344 **5.1 Source location of landslide signals**

345 Assuming that Event 1 to Event 3 originated from the slope of the CL, we performed a particle  
346 motion analysis within 1 Hz to 3 Hz of V03G (back azimuth:  $208^\circ$ ) to clarify their source locations. Given  
347 the surface behavior of the landslides, our analysis focused on the vertical and radial components  
348 associated with the propagation of Rayleigh waves. Regarding Event 1, we observed intricate patterns of  
349 particle motion, particularly during phase 1 of the sliding (Fig. S5). While the initial sliding phase of  
350 Event 1 indicated significant movement, the event was governed by a single force mechanism. However,  
351 not all materials involved in the landslide exhibited pure shear sliding. Some materials were bouncing,  
352 rolling, or interacting with the ground, slopes, and adjacent particles. These physical processes could  
353 generate high-frequency signals, resulting in complex and inexplicable particle motion patterns from  
354 phase 1 to phase 2 of Event 1. In contrast, the particle motion displayed a more consistent direction during  
355 the small-scale mass movement observed in phases 3 and 4, which manifested as clear ellipses. Notably,  
356 the ellipse corresponding to phase 3-II of Event 1 was particularly pronounced and linked to Events 2 and  
357 3 (Fig. 10). These elliptical patterns indicated retrograde motion along the travel direction.

358 Further, we investigated the relationship between different back azimuths and elliptical shapes.  
359 When the back azimuth was set at  $228^\circ$ , the elliptical shapes showed a noticeable change (Fig. S6a).  
360 However, similar elliptical shapes were consistently observed for back azimuth values ranging from  $188^\circ$   
361 to  $148^\circ$  (Figs. S6b-c). This suggests that elliptical shapes do not exhibit significant sensitivity within  $208^\circ$   
362 to  $148^\circ$ , where sources could potentially originate from a wide back azimuth range. Nevertheless, no  
363 documented landslides are reported during the range of back azimuth between  $208^\circ$  to  $148^\circ$  (Fig. S7);  
364 most substantial landslides are oriented with back azimuth angles greater than  $228^\circ$  (Fig. 2). Subsequently,  
365 the CC and ASL results indicated that Event 2 is close to V03G. Therefore, we posit that at least Event 1  
366 and Event 2 likely originated from the same source direction. Event 3, the minor event, challenges  
367 determining its precise location by seismic analysis.



368

369 Figure 10 Particle motion comparison between radial and vertical components for phase 3-II of Event 1,  
 370 Event 2, and Event 3. The duration of particle motion signals is indicated in the upper right corner of each  
 371 subfigure, with precise timing details highlighted by orange bars in Fig.4.

## 372 5.2 Comprehensive information from seismic analysis

373 When Event 1 and Event 2 occurred on the same slope, we estimated the approximate volume of  
 374 the CL using empirical regressions. Event 1 indicated a volume of 523,540 m<sup>3</sup> based on empirical  
 375 regression (mass = 0.405 × force magnitude; Chao et al., 2016) for large-scale landslides with a sliding  
 376 direction of 153.67° (Table 1). By retrieving the amplitude at the source (A<sub>0</sub>; unit: cm s<sup>-1</sup>) through 1-8 Hz  
 377 of horizontal signals, we estimated the volume of Event 2 is 16,791 m<sup>3</sup> (Volume= 77,290 A<sub>0</sub><sup>0.44</sup>; Chang  
 378 et al., 2021). The total volume obtained from a seismic analysis output of 540,331 m<sup>3</sup> is around 19%  
 379 lower than the volume estimated by the difference between LiDAR and DSM.

380 Seismic signal analysis provides valuable insight into potential landslide processes. The SF  
 381 method detailed the timing and movement direction. The DST spectrogram analysis revealed distinct  
 382 timeframes and physical patterns of the three events associated with slope failure. Event 1 likely involved  
 383 four sliding failures within 30 seconds with gradually decreasing masses. However, the landslide video  
 384 captured the process, lasting approximately 34 seconds for probable phases 2 and 3 in Event 1. This  
 385 discrepancy in timing may be attributed to the weak kinetic energy during the early and termination stages  
 386 of the CL. The ground vibration signal at those stages might not transmit to V03G, potentially influencing



387 the recorded duration. Subsequently, Event 2 featured 30s of continuous rockfall, followed by a toppling  
388 event with a larger mass.

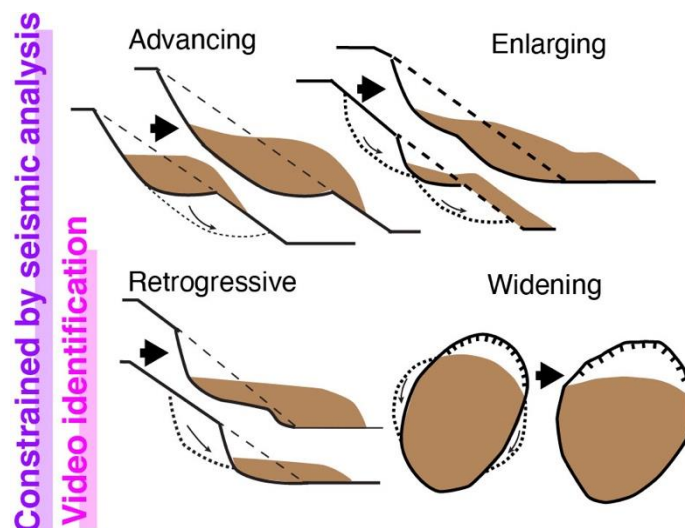
389 **Table 1** Pre-survey information of the CL by seismic analysis

<b>Landslide characteristics</b>	<b>Information</b>	
	Event 1	Event 2
Occurrence time	4:10 PM on 16 October 2022.	4:30 PM on 16 October 2022
Estimated volume	523,540 m <sup>3</sup>	16,791 m <sup>3</sup>
Sliding direction	153.67°	-
Failure process	Four continuous sliding with the gradual reduction in sliding volume	Rockfall and toppling

390

### 391 **5.3 Landslide evolution model**

392 Landslides are categorized into seven movement types (Varnes, 1978). According to the  
393 spectrogram features of Event 1 in the CL, this seismic analysis preferred sliding movement. The stepwise  
394 failure process of a landslide can be determined based on the distribution of landslide activity, such as  
395 advancing, retrogressive, enlarging, or widening activities (Fig. 11) (WP/WLI, 1993). Advancing and  
396 retrogressive activity involves the expansion of the rupture surface along and in the opposite direction of  
397 movement. Enlargement entails the rupture surface expanding in multiple directions, whereas widening  
398 indicates that the rupture surface extends into one or both flanks of the landslide.



399

400 Figure 11 Schematic diagram of potential landslide activities for the CL. Dot lines represent the  
401 detachments in the next stage. Dash lines indicate the original ground level. The brown color indicates  
402 the extent of displaced material. The figure has been modified from Cooper (2007).

403 For the CL, the left flank was exposed at the beginning of the video (Fig. S1), which implies  
404 previous failures had occurred earlier than the beginning of the video. It is reasonable that people were  
405 attracted by previous failures and prepared to take videos for subsequent failures. Besides, the debris flow  
406 had deposited a debris fan on the road (Fig. 2h), and excavators were operated to clear the buried road  
407 section. The moving mass from the upslope was sliding downward and pushing the previous colluvium.  
408 Moreover, some trees displaced to downslope on the top of moving mass, which implies a similar  
409 phenomenon during early failure with similar landslide source conditions (Fig. 7). Consequently, the  
410 video recorded the process of sliding that could correspond to the distribution and geometry of deposits  
411 (Figs. 7 and 8) and validate the sliding of Event 1 by seismic analysis (Fig. 4d).

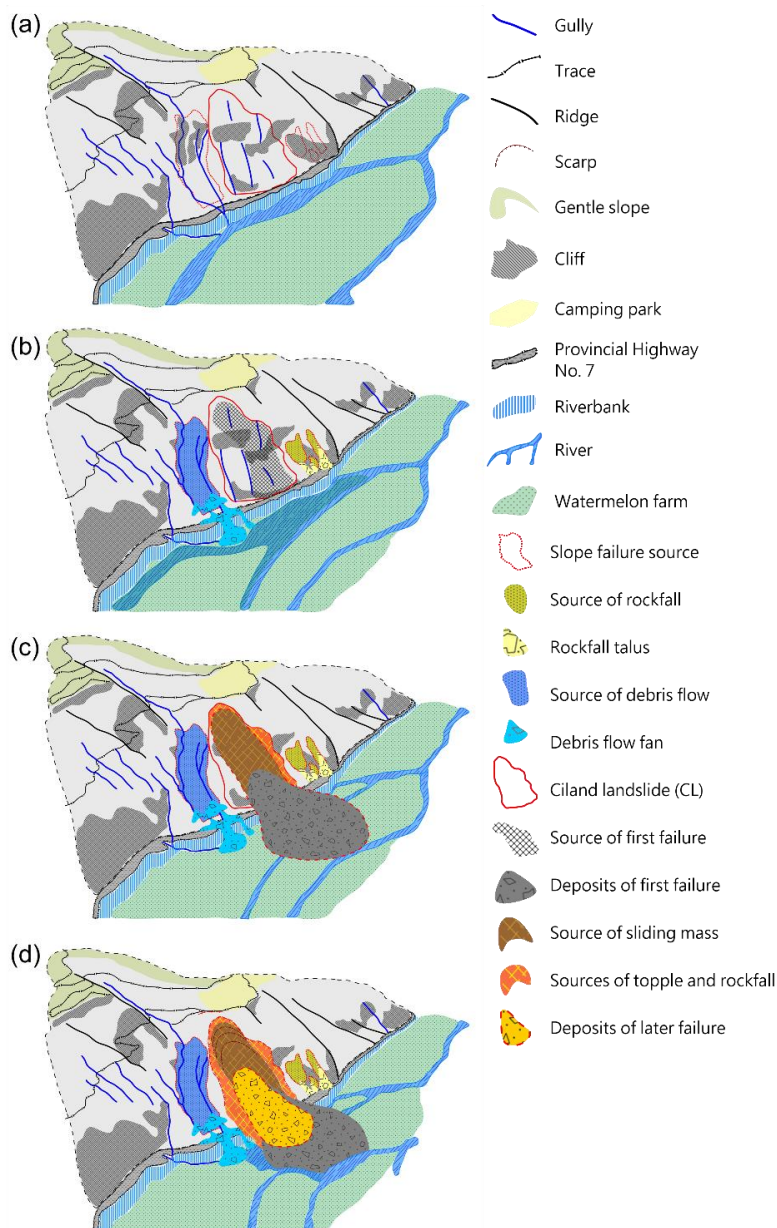
412 Combining the pre-survey understanding with the survey results, the initial model for landslide  
413 evolution was established (Fig. 12a). According to the announces of the Directorate General of Highways  
414 in Taiwan (Table S1) and the CL occurrence time extracted by seismic analysis, the debris flow and  
415 rockfall were induced by heavy rainfall before the CL (Fig. 12b). The initial failure mechanism of the CL  
416 could be assumed to initiate at a shear-off from the original toe (roadside slope) caused by the high pore-  
417 water pressure after heavy rainfall infiltration. The first failure should deposit on sandy and gravelly



418 alluvial deposits with high water levels (Fig. 12b). The rapid loading of sliding mass onto the wet alluvial  
419 deposits may have induced liquefaction and reduced the basal friction of sliding mass (Sassa, 1992). The  
420 first failure had the most significant volume, leading to higher mobility (Figs. 7, 8, and 12c) (Corominus,  
421 1996; Legros, 2002; Hungr and Evans, 2004). It possibly corresponds to Phase 1 of Event 1 in Table S1.  
422 However, for subsequent failures (Phases 2-4 of Event 1), failure masses were deposited on the angular  
423 debris and boulders of the previous colluvium, characterized by a rough ground surface, resulting in lower  
424 mobility (Fig. 12d). This process of retrogression may be captured in the video (Fig. S1). Therefore, the  
425 most plausible landslide activities could be retrogression in Event 1. Then, the widening activity  
426 developed by toppling and rockfalls with subsequent Event 2, Event 3, and other failures from the steep  
427 scarp and flanks (Fig. 11) (refers to YouTube video: <https://www.youtube.com/watch?v=PMIb7OiCqMQ>;  
428 last access on 2 April 2024).

429 The continuous presence of the four phases in Event 1 (Fig. 4b) and the field survey imply a  
430 fractured bedrock/steep sliding surface near the CL. Following the landslide, steep scarps and flanks  
431 emerged, exhibiting discontinuities such as cleavage, joints, and numerous tension cracks at the crown  
432 (Figs. 9f-9j). This observation suggests the potential for further enlargement of the landslide. An unstable  
433 slope directly threatened the safety of residents living close to the crown of the CL. Therefore, it is  
434 imperative to implement comprehensive monitoring measures on the slopes described by Kang et al.  
435 (2021). These measures are essential for gaining a deeper understanding of ongoing landslide activity and  
436 ensuring the safety of the affected population.





437

438 Figure 12 The geological model and topographic evolution of the CL. (a) The initial model is based on  
 439 LiDAR topographic features. (b) According to Fig. 2 and Table S1, slope failures (debris flow and  
 440 rockfalls) occurred around the CL. (c) The failure process of Phase 1 of Event 1 of the CL is based on  
 441 Figs. 4 and 7 and Table 1. (d) The final stage of the CL, after Phases 2-4 of Event 1, Events 2 and 3 of  
 442 the CL.



## 443 6. Conclusions

444 Research on the Cilan Landslide (CL) has shown how to deliver seismic analysis results as pre-  
445 survey knowledge to geologists for field surveys. We investigated a series of events involving the efficient  
446 generation of one-hour spectrograms through a discrete Fourier transform. Three events, Event 1, Event  
447 2, and Event 3, were identified, with four continuous phases of sliding, rockfall, and the subsequent  
448 toppling and rockfalls, as revealed by the spectrograms obtained via a Stockwell transform with a semi-  
449 log frequency axis. The initial sliding of the CL generated low-frequency seismic signals (ranging from  
450 0.02 Hz to 0.05 Hz), and we successfully determined an inverted single force direction of  $153.67^\circ$ , close  
451 to the actual direction of landslide movement, which was  $148^\circ$ . This geohazard location (GeoLoc)  
452 pinpointed Event 1 and Event 2 close to seismic station V03G, whereas a polarization analysis provided  
453 further support for the notion that these event sources may have originated from the same direction,  
454 indicating a high probability of sharing the same slope of origin. Additionally, by employing the force  
455 magnitude and amplitude at the source ( $A_0$ ) in the empirical regressions for Event 1 and Event 2 of the  
456 CL, we estimated the landslide volume to be  $540,331 \text{ m}^3$ , 19% lower than the volume calculated using a  
457 digital elevation model.

458 This information has significantly contributed to geologists' understanding of the physical  
459 processes underlying the CL for predicting advancing, retrogressive, enlarging, or widening mechanisms.  
460 After combining the field survey, the seismic analysis results have led geologists to propose a detailed  
461 mechanism for the CL. This mechanism involves shear-off from the roadside slope and subsequent mass  
462 sliding triggered by high pore-water pressure from rainfall infiltration. The observed physical behaviors  
463 of subsequent failures and topographic features with imbrication-like deposits suggest that the most  
464 plausible landslide activity may undergo retrogression and widening over time.

465 The research supported the idea that seismic analysis enables the determination of a landslide's  
466 inverted-force direction, estimated landslide volume, and physical processes. Notably, seismic analysis  
467 from an adjacent station provides additional temporal insight into landslides' dynamics, whereas  
468 geological surveys can only investigate the topography post-landslide to constrain the failure mechanisms.  
469 Therefore, seismic analysis provides crucial information for geologists before conducting field surveys.



#### 470 **Data availability**

471 Waveform data for this study were provided by the Broadband Array in Taiwan for Seismology (BATS;  
472 <https://doi.org/10.7914/SN/TW>, Academia Sinica, Institute of Earth Sciences, 1996.) and the Central  
473 Weather Administration, Taiwan (CWA; <https://doi.org/10.7914/SN/T5>). The raw seismic data of V03G  
474 is available through Figshare (<https://doi.org/10.6084/m9.figshare.24464281.v1>). The digital terrain  
475 model (DTM) of the 20-meter resolution used in Fig. 2 is available from the Government Open Data  
476 Platform, Taiwan (<https://data.gov.tw/dataset/35430>; Ministry of the Interior, 2024). The road shape files  
477 are available from the National Land Surveying and Mapping Center, Taiwan  
478 ([http://maps.nlsc.gov.tw/S\\_Maps/wms](http://maps.nlsc.gov.tw/S_Maps/wms)). The last accessed of all URLs was on 4 April 2024.

#### 479 **Competing interests**

480 The contact author has declared that none of the authors has competing interests.

#### 481 **Author contribution**

482 JM and CM conceived of the presented idea. WA supervised the project and provided critical feedback  
483 and helped shape the research, analysis and manuscript. JM, CM, WA, MW carried out the field  
484 investigations. CS, MW, TC, and CY discussed the results and contributed to the final manuscript.

#### 485 **Acknowledgments**

486 The authors acknowledged the National Science and Technology Council of Taiwan (NSTC) for the  
487 funding support. The authors acknowledge the Forestry and Nature Conservation Agency, Taiwan for  
488 providing LiDAR data and the Geological Survey and Mining Management Agency, Taiwan for LiDAR  
489 data establishment.

#### 490 **Financial support**

491 This study is financially supported by the National Science and Technology Council of Taiwan (NSTC)  
492 for Che-Ming Yang under grants NSTC 110-2116-M-239-001-MY2, NSTC- 112-2116-M-239-001,  
493 NUU project No. SM113004 and We-An Chao under grants NSTC 111-2625-M-A49-004-MY3.



## 494 **References**

- 495 Agliardi, F., Crosta, G., and Zanchi, A.: Structural constraints on deep-seated slope deformation  
496 kinematics, *Eng. Geol.*, 59(1-2), 83-102, [https://doi.org/10.1016/S0013-7952\(00\)00066-1](https://doi.org/10.1016/S0013-7952(00)00066-1), 2001.
- 497 Aki, K. and Ferrazzini, V.: Seismic monitoring and modeling of an active volcano for prediction, *J.*  
498 *Geophys. Res.*, 105, 16617–16640, <https://doi.org/10.1029/2000JB900033>, 2000.
- 499 Allstadt, K.: Extracting source characteristics and dynamics of the August 2010 Mount Meager landslide  
500 from broadband seismograms, *J. Geophys. Res.*, 118, 1472–1490, <https://doi.org/10.1002/jgrf.20110>,  
501 2013.
- 502 Brodsky, E. E., Gordeev, E., and Kanamori, H.: Landslide basal friction as measured by seismic waves,  
503 *Geophys. Res. Lett.*, 30, 2236, <https://doi.org/10.1029/2003GL018485>, 2003.
- 504 Chang, J.M., Chao, W.A., Chen, H., Kuo, Y.T., and Yang, C.M.: Locating rock slope failures along  
505 highways and understanding their physical processes using seismic signals, *Earth Surf. Dynam.*, 9,  
506 505–517, <https://doi.org/10.5194/esurf-9-505-2021>, 2021.
- 507 Chang, J.M., Chao, W.A., Kuo, Y.T., Yang, C.M., Chen, H., and Wang, Yu.: Field experiments: How  
508 well can seismic monitoring assess rock mass falling? *Eng. Geol.*, 323, 107211,  
509 <https://doi.org/10.1016/j.enggeo.2023.107211>, 2023.
- 510 Chao, W.A., Zhao, L., Chen, S.C., Wu, Y.M., Chen, C.H., and Huang, H.H.: Seismology-based early  
511 identification of dam-formation landquake events, *Sci. Rep.*, 6, 19259,  
512 <https://doi.org/10.1038/srep19259>, 2016.
- 513 Chao, W.A., Wu, Y.M., Zhao, L., Chen, H., Chen, Y.G., Chang, J.M., and Lin, C.M.: A first near real-  
514 time seismology-based landquake monitoring system, *Sci. Rep.*, 7, 43510,  
515 <https://doi.org/10.1038/srep43510>, 2017.
- 516 Chao, W.A., Wu, T.R., Ma, K.F., Kuo, Y.T., Wu, Y.M., Zhao, L., Chung, M.J., Wu, H., and Tsai, Y.L.:  
517 The large Greenland landslide of 2017: Was a tsunami warning possible? *Seismol. Res. Lett.* 89(4),  
518 1335-1344. <https://doi.org/10.1785/0220170160>, 2018.



- 519 Chen, C.-H., Chao, W.A., Wu, Y.M., Zhao, L., Chen, Y.G., Ho, W.Y., Lin, T.L., Kuo, K.H., and Chang,  
520 J.M.: A seismological study of landquakes using a real-time broad-band seismic network, *Geophys.*  
521 *J. Int.*, 194, 885–898, <https://doi.org/10.1093/gji/ggt121>, 2013.
- 522 Chen, L.C.: Action Plan for Prevention and Control of Large-Scale Landslide Disasters (In Chinese),  
523 National Science and Technology Center for Disaster Reduction, Taiwan, <https://reurl.cc/M8anXL>,  
524 2015.
- 525 Chigira, M.: Long-term gravitational deformation of rocks by mass rock creep. *Eng. Geol.*, 32, 157-184,  
526 [https://doi.org/10.1016/0013-7952\(92\)90043-X](https://doi.org/10.1016/0013-7952(92)90043-X), 1992.
- 527 Cooper, R.G. 2007. Mass Movements in Great Britain, Geological Conservation Review Series, No. 33,  
528 Joint Nature Conservation Committee, Peterborough, 348 pp.
- 529 Dietze, M., Turowski, J. M., Cook, K. L., and Hovius, N.: Spatiotemporal patterns, triggers and anatomies  
530 of seismically detected rockfalls, *Earth Surf. Dynam.*, 5, 757–779, [https://doi.org/10.5194/esurf-5-](https://doi.org/10.5194/esurf-5-757-2017)  
531 [757-2017](https://doi.org/10.5194/esurf-5-757-2017), 2017.
- 532 Ekström, G. and Stark, C. P.: Simple scaling of catastrophic landslide dynamics, *Science*, 339, 1416–  
533 1419, <https://doi:10.1126/science.1232887>, 2013.
- 534 Fei, L.Y., Chen, M.M.: Geological investigation and database construction for upstream of flood-prone  
535 area – maps and explanatory text (In Chinese). Central Geological Survey, MOEA, Taiwan, 192,  
536 2013.
- 537 Feng, Z.: The seismic signatures of the 2009 Shiaolin landslide in Taiwan, *Nat. Hazards Earth Syst. Sci.*,  
538 11, 1559–1569, <https://doi.org/10.5194/nhess-11-1559-2011>, 2011.
- 539 Fuchs, F., Lenhardt, W., Bokelmann, G., and the AlpArray Working Group: Seismic detection of  
540 rockslides at regional scale: examples from the Eastern Alps and feasibility of kurtosis-based event  
541 location, *Earth Surf. Dynam.*, 6, 955–970, <https://doi.org/10.5194/esurf-6-955-2018>, 2018.
- 542 Guinau, M., Tapia, M., Pérez-Guillén, C., Suriñach, E., Roig, P., Khazaradze, G., Torné, M., Royán, M.  
543 J., and Echeverria, A.: Remote sensing and seismic data integration for the characterization of a rock



- 544 slide and an artificially triggered rock fall, *Eng. Geol.*, 257, 105113,  
545 <https://doi.org/10.1016/j.enggeo.2019.04.010>, 2019.
- 546 Dammeier, F., Moore, J.R., Haslinger, F. and S. Loew: Characterization of alpine rockslides using  
547 statistical analysis of seismic signals, *J. Geophys. Res.*, 116, F04024,  
548 <https://doi:10.1029/2011JF002037>, 2011.
- 549 Hibert, C., Ekström, G., and Stark, C. P.: Dynamics of the Bingham Canyon Mine landslides from seismic  
550 signal analysis, *Geophys. Res. Lett.*, 41, 4413-4804, <https://doi.org/10.1002/2014GL060592>, 2014.
- 551 Hibert, C., Stark, C. P., and Ekström, G.: Dynamics of the Oso-Steelhead landslide from broadband  
552 seismic analysis, *Nat. Hazards Earth Syst. Sci.*, 15, 1265–1273, [https://doi.org/10.5194/nhess-15-](https://doi.org/10.5194/nhess-15-1265-2015)  
553 [1265-2015](https://doi.org/10.5194/nhess-15-1265-2015), 2015.
- 554 Hungr, O., and Evans, S.G.: Entrainment of debris in rock avalanches: An analysis of a long run-out  
555 mechanism. *GSA Bulletin*, 116 (9-10), 1240–1252. <https://doi.org/10.1130/B25362.1>, 2004.
- 556 Hungr, O., Leroueil, S., and Picarelli, L.: The Varnes classification of landslide types, an update.  
557 *Landslides* 11, 167–194, <https://doi.org/10.1007/s10346-013-0436-y>, 2014.
- 558 Kanamori, H., and Given, J. W.: Analysis of long-period seismic waves excited by the May 18, 1980,  
559 eruption of Mount St. Helens - A terrestrial monopole?, *J. Geophys. Res.*, 87, 5422–5432,  
560 [doi:10.1029/JB087iB07p05422](https://doi.org/10.1029/JB087iB07p05422), 1982.
- 561 Kang, K.H., Chao, W.A., Yang, C.M., Chung, M.C., Kuo, Y.T., Yeh, C.H, Liu, H.C., Lin, C.H., Lin, C.P.,  
562 Liao, J.J., Chang, J.M., Ngui, Y.N., and Tai, T.L.: Rigidity Strengthening of Landslide Materials  
563 Measured by Seismic Interferometry. *Remote Sens.* 13(14), 2834.  
564 <https://doi.org/10.3390/rs13142834>, 2021.
- 565 Kao, H., Jian, P.R., Ma, K.F., Huang, B.S. and Liu, C.C.: Moment-tensor inversion for offshore  
566 earthquakes east of Taiwan and their implications to regional collision. *Geophys. Res. Lett.*, 25,  
567 3619-3622. <https://doi.org/10.1029/98GL02803>, 1998.



- 568 Kuo, H.L., Lin, G.W., Chen, C.W., Saito, H., Lin, C.W., Chen, H., and Chao, W.A.: Evaluating critical  
569 rainfall conditions for large-scale landslides by detecting event times from seismic records, *Nat.*  
570 *Hazards Earth Syst. Sci.*, 18, 2877–2891, <https://doi.org/10.5194/nhess-18-2877-2018>, 2018.
- 571 Legros, F.: The Mobility of Long-Runout Landslides. *Eng. Geol.*, 63, 301-331.  
572 [http://dx.doi.org/10.1016/S0013-7952\(01\)00090-4](http://dx.doi.org/10.1016/S0013-7952(01)00090-4), 2002.
- 573 Manconi, A., Mondini, A. C., and the AlpArray working group: Landslides caught on seismic networks  
574 and satellite radars, *Nat. Hazards Earth Syst. Sci.*, 22, 1655–1664, [https://doi.org/10.5194/nhess-22-](https://doi.org/10.5194/nhess-22-1655-2022)  
575 [1655-2022](https://doi.org/10.5194/nhess-22-1655-2022), 2022.
- 576 Moretti, L., Mangeney, A., Capdeville, Y., Stutzmann, E., Huggel, C., Schneider, D., and Bouchut, F.:  
577 Numerical modeling of the mount Steller landslide flow history and of the generated long period  
578 seismic waves. *Geophys. Res. Lett.*, 39, L16402, <https://doi.org/10.1029/2012GL052511>, 2012.
- 579 Provost, F., Malet, J.-P., Hibert, C., Helmstetter, A., Radiguet, M., Amitrano, D., Langet, N., Larose, E.,  
580 Abancó, C., Hürlimann, M., Lebourg, T., Levy, C., Le Roy, G., Ulrich, P., Vidal, M., and Vial, B.:  
581 Towards a standard typology of endogenous landslide seismic sources, *Earth Surf. Dynam.*, 6, 1059-  
582 1088, <https://doi.org/10.5194/esurf-6-1059-2018>, 2018.
- 583 Sassa, K.: Landslide volume–apparent friction angle relationship in the case of rapid loading on alluvial  
584 deposits. *Landslide News* 6, 16 – 19, 1992.
- 585 Shin, T.C., and Chen, Y.L.: Study of earthquake location of 3-D velocity structure in Taiwan area. (In  
586 Chinese). *Meteorological Bulletin* 42, 135-169,  
587 <https://photino.cwb.gov.tw/rdcweb/lib/cd/cd07mb/MB/PDF/42/No.2/03.pdf>, 1998.
- 588 Suriñach, E., Vilajosana, I., Khazaradze, G., Biescas, B., Furdada, G., and Vilaplana, J. M.: Seismic  
589 detection and characterization of landslides and other mass movements, *Nat. Hazards Earth Syst.*  
590 *Sci.*, 5, 791–798, <https://doi.org/10.5194/nhess-5-791-2005>, 2005.



- 591 Varnes, D.: Slope movement types and processes. In *Landslides: Analysis and Control* (eds Schuster, R.  
592 L. & Krizek, R. J.), Transportation Research Board, National Academy of Science, Washington,  
593 1978.
- 594 Vilajosana, I., Suriñach, E., Abellán, A., Khazaradze, G., Garcia, D., and Llosa, J.: Rockfall induced  
595 seismic signals: case study in Montserrat, Catalonia, *Nat. Hazards Earth Syst. Sci.*, 8, 805–812,  
596 <https://doi.org/10.5194/nhess-8-805-2008>, 2008.
- 597 Walter, F., Burtin, A., McArdell, B. W., Hovius, N., Weder, B., and Turowski, J. M.: Testing seismic  
598 amplitude source location for fast debris-flow detection at Illgraben, Switzerland, *Nat. Hazards Earth*  
599 *Syst. Sci.*, 17, 939–955, <https://doi.org/10.5194/nhess-17-939-2017>, 2017.
- 600 Walsh, B., Jolly, A. D., and Procter, J.: Calibrating the amplitude source location (ASL) method by using  
601 active seismic sources: An example from Te Maari volcano, Tongariro National Park, New Zealand,  
602 *Geophys. Res. Lett.*, 44, 3591–3599, <https://doi.org/10.1002/2017GL073000>, 2017.
- 603 Weng, M.C., Lin, C.H., Shiu, W.J., Chao, W.A., Chiu, C.C., Lee, C.F., Huang, W.K., and Yang, C.M.:  
604 Towards a rapid assessment of highway slope disasters by using multidisciplinary techniques,  
605 *Landslides*, 19, 687–701, <https://doi.org/10.1007/s10346-021-01808-0>, 2022.
- 606 WP/ WLI. (International Geotechnical Societies UNESCO Working Party on World Landslide Inventory)  
607 1993. A suggested method for describing the activity of a landslide. *Bull. Eng. Geol.*, No. 47, 53-57.
- 608 Wu, Y.M., Chang, C.H., Zhao, L., Shyu, J.B.H., Chen, Y.G., Sieh, K., and Avouac, J.P.: Seismic  
609 tomography of Taiwan: improved constraints from a dense network of strong-motion stations, *J.*  
610 *Geophys. Res.: Solid Earth*, 112, B08312, <https://doi:10.1029/2007JB004983>, 2007.
- 611 Yamada, M., Kumagai, H., Matsushi, Y., and Matsuzawa, T.: Dynamic landslide processes revealed by  
612 broadband seismic records, *Geophys. Res. Lett.*, 40, 2998–3002, doi:10.1002/grl.50437, 2013.
- 613 Yang, C.M., Chang, J.M., Hung, C.Y., Lu, C.H., Chao, W.A. and Kang, K.H.: Life span of a landslide  
614 dam on mountain valley caught on seismic signals and its possible early warnings, *Landslides*, 19,  
615 637–646, <https://doi.org/10.1007/s10346-021-01818-y>, 2022.